Conference Note

tag: sPH-CONF-JET-2026-03
date: June 21, 2026

sPHENIX Conference Note

Measurement of the correlation between underlying event and jet production in $p+p$ collisions at $\sqrt{s} = 200$ GeV using the sPHENIX detector

The sPHENIX Collaboration

Abstract

Studying the interplay between jets originating from high-energy partonic scatterings and soft or low-energy particle production in the transverse region probes multi-parton interactions and initial- and final-state radiation in $p+p$ collisions. The transverse energy density in the underlying event (UE) is measured as a function of leading jet transverse momentum (p_T) in $p+p$ collisions at $\sqrt{s} = 200$ GeV using the sPHENIX detector, for both inclusive jet and dijet selections. A consistent decrease of the UE transverse energy density with increasing jet p_T is observed in both cases. The results are compared to predictions from Pythia8 and Herwig7, which implement different approaches in both the perturbative and non-perturbative sector. Pythia8 reproduces the observed trend, while Herwig7 predicts an approximately constant UE activity in the reported region, significantly diverging from the data at high jet p_T.

1 Introduction

In high-energy proton-proton collisions, hard partonic scatterings produce jets, while additional soft activity arises from multiple parton interactions (MPI), initial- and final-state radiation (ISR/FSR), and contributions from the hadronization of beam remnants and their associated color connections [1, 2, 3, 4]. This soft component, referred to as the underlying event (UE), can be studied as a function of the hard scattering scale, for example using the leading jet transverse momentum (p_T), providing insight into the interplay between the hard process and the underlying soft particle production. In this analysis, the UE is quantified using calorimetric measurements of energy deposits, clustered into topological clusters (topoclusters). Such measurements are essential for understanding how soft activity evolves with the energy scale of the interaction [5, 6] and, critically help in constraining models of soft particle production associated with jets in proton–proton collisions ($p + p$).

In a simplified picture, higher-Q^2 scatterings are expected to produce increased UE activity through enhanced radiation [7] and a greater likelihood of multiple parton interactions associated with more central proton–proton overlap [1, 8]. However, this expectation may be modified at lower collision energies, where phase space for radiation is reduced with high p_T jet production. Regardless of the underlying dynamics, at sufficiently high jet energies, energy conservation alone provides an inescapable mechanism that would reduce particle production in the UE. Measurements at the Relativistic Heavy Ion Collider (RHIC) therefore provide a unique opportunity to test the extent to which soft particle production follows or deviates from this well-defined picture at the Large Hadron Collider (LHC) collision energies [9, 10, 11].

To study the UE as a function of the hard scattering, jet events are characterized using the event shape first introduced by the CDF experiment [12]. The azimuthal plane is divided into "towards," "away," and "transverse" regions relative to the leading jet direction, with the transverse region providing sensitivity to UE activity. Figure 1 illustrates this event geometry, showing the azimuthal segmentation relative to the leading jet axis.

Previous measurements at RHIC have shown that the UE activity in inclusive jet events exhibits a weak or decreasing dependence on the hard scale [13, 14], in contrast to measurements at the LHC, where the UE typically increases with the leading jet p_T [9, 10, 11]. This difference can be explained in part by the larger phase space available for ISR and FSR at higher beam energies, as well as a kinematic coupling of the hard and soft scales arising due to energy-momentum conservation effects that redistribute energy across different rapidity regions [15, 16]. When a dijet selection is imposed, LHC measurements show a reduced or slightly negative dependence of the UE on the hard scale, similar to observations at RHIC [13]. These results highlight the sensitivity of UE observables to both collision energy and event selection.

The high-statistics $p + p$ dataset collected by the sPHENIX [17] experiment during RHIC Run 2024 enables measurements of jet observables up to large leading jet p_T at RHIC [18]. This dataset extends current measurements of correlations between jet production and UE, to events involving large parton momentum fractions (up to $x \approx 0.6$). This measurement reports the UE in the transverse region for leading jet p_T range of 21–63.5 GeV using a sample of $p + p$ collisions corresponding to an integrated luminosity of approximately 34 pb^{-1}.

In this note, the UE is reported as a function of leading jet p_T in both inclusive jet and dijet events,

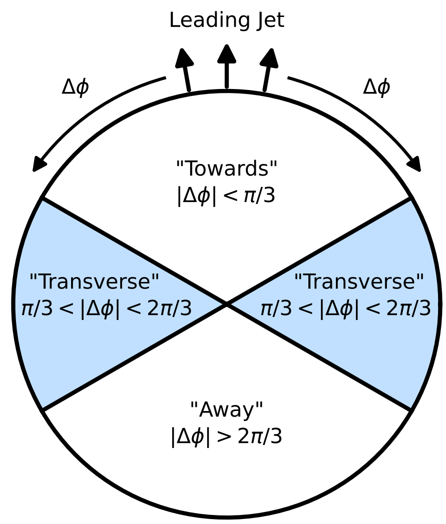

Figure 1: Schematic of ”towards”, ”transverse”, and ”away” regions of jet event where regions are defined by their $|\Delta\phi|$ with respect to the leading jet ϕ.

allowing for a direct comparison of event selection effects. The results are further compared to predictions from event generators such as Pythia8 [19, 20] and Herwig7 [21, 22], which employ different approaches to modeling the interplay between multi-parton interactions, parton showers, and hadronization mechanisms.

2 sPHENIX Detector

sPHENIX [17] is a new experiment designed to measure jet and heavy-flavor probes of the quark gluon plasma (QGP) created in Au+Au collisions at the Relativistic Heavy-Ion Collider (RHIC) [23]. In addition to its heavy-ion program, sPHENIX carries out a high-statistics $p+p$ program that provides essential reference measurements for the heavy-ion results and enables a broad range of small system and jet physics studies in its own right. The electromagnetic and hadronic calorimeter system is crucial for measuring the energy of jets and identifying direct photons and electrons.

Moving outwards from the beam line, sPHENIX comprises the electromagnetic calorimeter (EMCal) [24, 25], the inner hadronic calorimeter (IHCal) [25], the 1.4 T superconducting solenoid magnet [26], and the outer hadronic calorimeter (OHCal) [25]. These detectors have full azimuthal coverage and span $|\eta| < 1.1$ in pseudorapidity. sPHENIX also includes a number of forward detectors, namely the Minimum Bias Detectors (MBD) formerly known as the PHENIX Beam-Beam Counters [27, 28], the sPHENIX Event Plane Detectors (sEPD), and the Zero Degree Calorimeters (ZDC) which include the Shower Maximum Detector (SMD).

The sPHENIX EMCal [24, 25] is 20.1 radiation lengths deep and is designed to measure photons, electrons, and positrons via electromagnetic showers. The sPHENIX EMCal is a sampling calorimeter made of a tungsten powder absorber and scintillating fibers with tower size $\Delta\eta \times \Delta\phi = 0.024 \times 0.024$. The light from the scintillating fibers is collected by a light guide and converted into a charge signal by silicon photomultipliers (SiPMs), which is subsequently amplified into a voltage signal by the readout electronics. The EMCal also measures 0.83 hadronic interaction lengths in depth and therefore records a significant fraction of hadronic shower energy on average.

The sPHENIX HCal system is designed to measure hadronic showers with the full EMCal + HCal system totaling 4.9 hadronic interaction lengths. Both the IHCal and OHCal are sampling calorimeters comprising aluminum (inner)/steel (outer) absorbing plates and scintillating tiles with tower size $\Delta\eta \times \Delta\phi = 0.1 \times 0.1$. Both IHCal and OHCal scintillating tiles are set at an angle offset to the transverse direction to reduce the amount of channeling effect in which the traversing particles may pass through the calorimeter only through the scintillation layer. The light from these tiles is then detected by SiPMs [25]. The calibration and reconstruction details for the sPHENIX EMCal and HCal follow the same procedure as outlined in Ref. [29]. sPHENIX recently measured the energy density across rapidity at top RHIC energy ($\sqrt{s_{NN}} = 200$ GeV) [30], with this reference detailing the calibration and uncertainties of the calorimeter subsystems.

This analysis uses data from all three calorimeters as well as collision vertex event information from the MBD. The MBD [28] is located at forward rapidity, $3.5 < |\eta| < 4.6$, on both sides of the interaction point, close to the beam pipe, and comprises 128 channels of photomultiplier tubes (PMTs). The MBD is used for triggering on minimum-bias (MB) events and for collision vertex determination. Minimum-bias events are defined here as inelastic p+p collisions satisfying the MBD trigger requirement of at least one fired channel on either side of the interaction point.

3 Analysis Procedure

3.1 Trigger Selection

The data used in this analysis were collected in $p + p$ collisions at $\sqrt{s} = 200$ GeV during RHIC Run 2024 and comprises two running periods: a period with zero beam crossing angle and a wide z_{vtx} distribution ($\sim$ 60 cm), and a period with a 1.5 mrad crossing angle and narrower distribution ($\sim$ 20 cm). All events included in the analysis were collected under physics data-taking conditions with the magnet on and stable detector operation. This analysis uses data combined from both running periods with consistent results across them both. Jet events are identified using a sliding window algorithm that scans partially overlapping regions of size $\Delta\eta \times \Delta\phi = 0.8 \times 0.8$ across the full calorimeter acceptance and records the maximum transverse energy (E_T) deposited across the windows within each event. The primary trigger used in this analysis corresponds to approximately $E_T > 10$ GeV within the window.

Additional quality requirements are imposed on the calorimeter system, including limits on cold, dead, and hot towers, as well as constraints on the timing response of each calorimeter subsystem to ensure stable signal reconstruction. Events are also required to have a reconstructed MBD vertex within $|z_{\text{vtx}}| < 60$ cm to ensure uniform detector acceptance and calorimeter response. Finally, to reduce contamination from pileup effects on the UE measurement, only events from running conditions with the mean number of inelastic collisions per bunch crossing $\mu < 0.11$ were used, limiting the overall rate of double interactions included in the final dataset. After all selections, the analyzed sample corresponds to an integrated luminosity of approximately 34 pb^{-1}, with the pileup and z_{vtx} cuts being the largest contributors to the reduction in the dataset.

3.2 Simulation Samples

Simulation samples are generated using Pythia8 [19] with a RHIC-tuned parameter set constrained by previous measurements at $\sqrt{s} = 200$ GeV [20], including both hard QCD processes and prompt photon production. A Herwig7 [21] simulation sample also tuned to measurements in $\sqrt{s} = 200$ GeV $p + p$ collisions at RHIC [22] is used to study model dependence in the analysis procedure and for direct comparison to results. The generated events are propagated through a full Geant4 [31] simulation of the sPHENIX detector and reconstructed using the same software chain as the data.

To provide sufficient statistical coverage across a wide range of jet transverse momenta, multiple simulated datasets are produced with different minimum momentum transfer thresholds. These samples cover a range in leading jet p_T from 7 GeV to 85 GeV and span many orders of magnitude in cross section. The samples are combined using weights proportional to their production cross sections divided by the number of generated events. Each dataset contains approximately 10^7 events.

3.3 Event and Jet Selection

The underlying event is studied using both inclusive jet and dijet event selections. Jets are built from inputs consisting of calorimeter towers with segmentation $\Delta\phi \times \Delta\eta = 0.1 \times 0.1$. These inputs include towers from the IHCal and OHCal as well as EMCal pseudo-towers combined into regions matching the HCal segmentation.

The jet reconstruction is described in detail in [32] and is summarized here. Anti-k_t [33, 34] jets are reconstructed with radius parameter $R = 0.4$ without any underlying event subtraction. Reconstruction and detector level jets are calibrated using a MC-based Jet Energy Scale (JES) and in simulation, an additional Jet Energy Resolution (JER) smearing factor is applied to match the resolution seen in data [32]. For both the inclusive jet and dijet event selection, the leading jet is required to lie within $|\eta| < 0.7$, ensuring full containment within the calorimeter acceptance, and must have a calibrated transverse momentum $p_T^{\text{lead}} > 21$ GeV. The dijet event selection additionally requires the presence of a second jet with p_T greater than 30% of the leading jet p_T and an azimuthal separation satisfying $\Delta\phi > 3\pi/4$. This sub-leading jet is also required to lie within $|\eta| < 0.7$. Finally, the dijet event selection requires that there be no additional jet outside of the leading and sub-leading jets in the event with p_T greater than 50% of the leading jet p_T [9]. The simulated vertex distribution is reweighted to match that observed in data and the calorimeter noise modeling is tuned to reproduce the conditions measured during Run 2024. These simulations are then used to construct response matrices for unfolding procedures, and to derive the MBD vertex reconstruction efficiency.

To suppress non-collision backgrounds, such as beam-related and high-energy cosmic ray backgrounds, additional jet quality requirements are applied. For the inclusive jet selection, these requirements include constraints on the fraction of jet energy deposited in different calorimeter subsystems. The fractions of jet energy deposited in the EMCal and OHCal are each required to lie between 10% and 90% of the total jet energy, while the energy fraction deposited in the IHCal must be less than 90%. This energy fraction cut is also applied at the reconstruction level in simulation and is corrected back to an unbiased inclusive jet distribution via the unfolding procedure, as described in detail in Section 3.5. The unfolding accounts for detector effects through a response matrix that includes the treatment of inefficiencies (missed truth jets) and fake reconstructed jets. The inclusive jet selection also applies timing-based jet quality selections on the leading jet time and correlations between the leading jet time and MBD time event-by-event. For the dijet selection, the jet quality requirements additionally include a timing-based selection on the time difference between the leading and sub-leading jet times. These timing cuts are designed to remove beam-related and cosmic ray backgrounds while maintaining high signal efficiency and purity.

The jet trigger efficiency is evaluated as a function of the reconstructed leading jet p_T using a data-driven approach. The efficiency is determined by comparing the jet yield selected with the jet trigger to that obtained from a minimum bias sample. The resulting efficiency curve is parameterized and used to derive event-by-event correction factors as a function of leading jet p_T. The resulting correction is 3% in events with $p_{T,\mathrm{lead}} = 21$ GeV and $< 1\%$ for events with $p_{T,\mathrm{lead}} > 24$ GeV.

Since the requirement of an MBD coincidence at forward rapidity could modify the transverse region ΣE_T production, the efficiency for reconstructing a valid event vertex using the MBD is evaluated in simulation as a function of leading jet p_T and transverse region total topocluster E_T (ΣE_T, defined below), and is found to vary by less than 5% across the measured ΣE_T range. Correction factors as a function of ΣE_T are applied to the unfolded distribution and result in an overall $\sim 1\%$ effect on the average transverse region ΣE_T.

3.4 Topological Clustering

A topological clustering algorithm is applied to calorimeter towers to reconstruct energy deposits from particle showers, forming topological clusters (topoclusters). Topological clustering is designed to reconstruct particle-induced energy deposits by grouping individual calorimeter tower signals into contiguous, three-dimensional clusters while suppressing electronic noise and pile-up contributions. The algorithm is based on the topological clustering approach developed by ATLAS [35], with adaptations specific to the sPHENIX calorimeter system, and begins by evaluating a signal-to-noise significance metric for each tower, defined as the tower's measured energy (E_{tower}) at the electromagnetic scale divided by its expected noise.

Topoclusters are then grown around towers with high significance in the following way. The clustering has three significance thresholds, denoted $\{S, N, P\}$ and defined in units of the tower noise (σ_{noise}, described in Section 3.4.1), which is determined via a procedure described below.

- Seed threshold (S): Towers with $|E_{\mathrm{tower}}| > S \cdot \sigma_{\mathrm{noise}}$ initiate clusters, with $S = 4$.
- Neighbor growth threshold (N): Adjacent towers with $|E_{\mathrm{tower}}| > N \cdot \sigma_{\mathrm{noise}}$ are iteratively added to expand the cluster, with $N = 2$.
- Peripheral threshold (P): All boundary towers bordering the neighboring towers, $P = 0$, are include to capture the full shower energy while allowing positive and negative noise contributions to cancel.

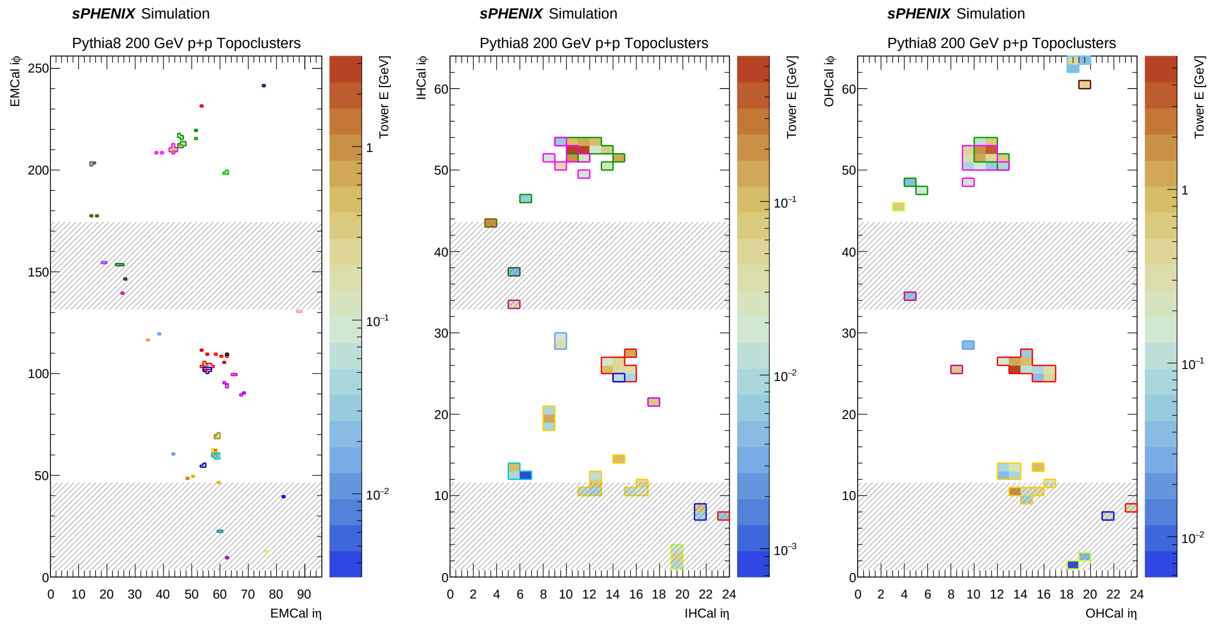

Figure 2: Display of topocluster boundaries (colored line borders) across the EMCal (left), IHCal (middle) and OHCal (right) calorimeter layers for a simulated $p+p$ dijet event in PYTHIA8. Each panel shows a rolled-out projection of the calorimeter acceptance, with the tower pseudorapidity index $i\eta$ on the horizontal axis and the tower azimuthal index $i\phi$ on the vertical axis, where $i\eta$ and $i\phi$ denote the integer tower indices corresponding to tower center positions. Tower energies in GeV are indicated by the fill color, with the scale shown by the color axis on the right. The dijet transverse region for this event is shown in gray shading.

The growth procedure outwards from seed towers is iterative, with neighboring towers defined as those adjacent in either η or ϕ within the same calorimeter layer, or overlapping in the (η, ϕ) plane across layers (EMCal, IHCal, and OHCal). Any neighboring tower satisfying the N threshold is added to the cluster and can itself seed further neighbors, expanding the cluster until no additional towers meet the criteria. Boundary towers at the P threshold are then included to capture the full shower shape with minimal noise contamination. In cases where a peripheral tower is adjacent to multiple clusters, it is uniquely assigned to a single cluster following the cluster growth ordering, ensuring that no tower is shared between clusters. An example of topocluster growth is shown in the distribution of topoclusters in a simulated dijet event display (Figure 2). Importantly, this cluster formation ordering of seed, neighboring, and peripheral towers makes topoclusters far less sensitive to noise than traditional distance-based clustering, since isolated noise fluctuations typically fail the seed threshold, and lower-significance noise towers are excluded unless supported by adjacent high-significance signals.

3.4.1 Topocluster resolution

The layer-dependent topocluster noise thresholds, σ_{noise}, are optimized for the calorimeter noise conditions measured during the Run 2024 $p+p$ data-taking period. A single noise threshold is used across the full calorimeter acceptance: the tower-by-tower pedestal RMS values, σ_{noise}.

These values are extracted from dedicated pedestal runs without collisions, with default values of $\sigma_{\text{noise}} = 68.4\,\text{MeV}$ for the EMCal, 5.3 MeV for the IHCal, and 35.1 MeV for the OHCal. These values are the maximum tower RMS for each calorimeter layer, which encompass 99.9% of the tower-by-tower RMS values. Simulation studies of isolated single particles in minimum-bias Pythia8 events with embedded realistic calorimeter noise are used to evaluate the reconstruction configuration. This is done by matching truth particles to topoclusters to characterize the resulting topocluster energy resolution. The resolution of topoclusters is studied separately for electromagnetic (EM) particles and hadrons. For the EM case, truth particles with $E > 1\,\text{GeV}$ are matched to clusters within $\Delta R < 0.1$, while for hadronic particles, truth particles with $E > 3\,\text{GeV}$ are matched within $\Delta R < 0.2$. The resolution is quantified using the relative width of the E/p ratio, where E is the topocluster energy and p is the momentum of the matched truth particle.

For reference, in the EMCal the default threshold corresponds to approximately 0.25 MIP equivalent energy, such that the seed threshold ($S = 4$) is close to one MIP, providing a physically well-motivated working point for noise suppression and signal retention. Figure 3 shows the E/p distributions for EM and hadronic particles using these thresholds. The extracted resolutions from the Gaussian fits in Figure 3 are 13.4% for 1 GeV EM particles and 50.8% for 3 GeV hadronic particles, in good agreement with expectations from EMCal and HCal test beam measurements [24, 25]. Resolutions for thresholds shifted up and down by the average of the tower-by-tower pedestal RMS distribution from the nominal value were also studied: the lower threshold resulted in a broader relative width of the E/p distribution, while the higher threshold did not significantly improve the E/p relative width and reduced the matching efficiency between truth particles and topoclusters. These variations are used to estimate the sensitivity of the topocluster resolution to the noise threshold.

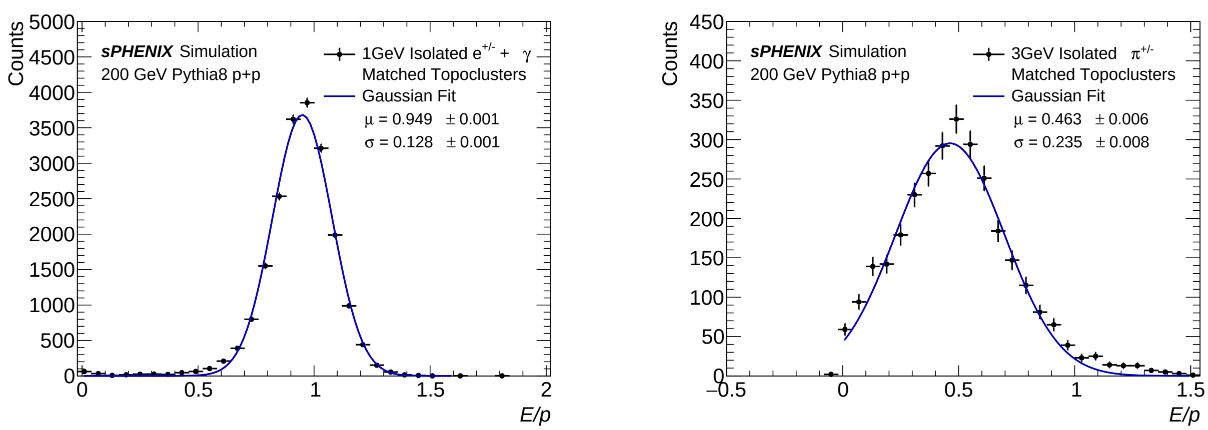

(a) EM particles ($E > 1\,\text{GeV}$, $\Delta R < 0.1$) **(b)** Hadrons ($E > 3\,\text{GeV}$, $\Delta R < 0.2$)

Figure 3: E/p distributions for EM particles(left) and hadrons (right) using the optimal topocluster noise thresholds for Run 2024 $p + p$ noise conditions. The distributions are shown for isolated single particles in Minimum-Bias $p + p$ Pythia8 + Geant4 simulation events.

3.4.2 Topocluster Energy Distribution

The mean total transverse energy density in the transverse region, $\langle \Sigma E_T/\delta\eta\delta\phi \rangle$, is constructed by summing the E_T from topoclusters with $E > -1$ GeV in the transverse region, $\pi/3 < \Delta\phi < 2\pi/3$ from the leading jet, and across the full calorimeter region $|\eta| < 1.1$. This quantity is first measured at the reconstruction level for inclusive jet and dijet events passing all jet quality cuts and using the kinematic and event selections outlined in Section 3.3. The topocluster energy cut of $E > -1$ GeV is applied to eliminate large noise and out-of-time pileup contributions but allow the contribution from negative-energy fluctuations to cancel with positive-energy fluctuations. Reconstruction-level comparisons between data and simulation are performed to validate the modeling of the detector response to both jet and underlying event observables. Figure 4 directly compares the reconstruction-level topocluster $\Sigma E_T/\delta\eta\delta\phi$ distributions between data and simulation events from the Pythia8 + Geant4 production for the transverse region. In general, good agreement is observed in the shape of the total transverse energy density distributions, $\Sigma E_T/\delta\eta\delta\phi$, reconstructed from topoclusters across all event regions, providing confidence in the use of the simulation to derive detector corrections.

Pileup effects are evaluated by studying the relationship between the run-by-run in-time pileup rate, determined from the minimum-bias collision rate, and the average transverse region total E_T, which exhibits an approximately linear increase with pileup rate at low pileup. A pileup correction obtained from the slope of a linear fit to dijet events is applied to the reconstructed transverse region E_T prior to unfolding, and is found to be consistent with a correction derived from inclusive jet events. This pileup correction changes the scale of the mean reconstructed E_T in the transverse region by $\sim 2.5\%$ across all leading jet p_T bins in both the dijet and inclusive jet samples indicating a non-negligible, but modest, effect on the UE measurement.

3.5 Unfolding Procedure

To correct for detector effects and extract particle-level observables, a two-dimensional unfolding procedure is performed for leading jet p_T and transverse region ΣE_T simultaneously. This unfolding accounts for bin migration effects arising from finite detector resolution in both jet p_T and calorimeter E_T and maintains correlations between the jet p_T and calorimeter E_T information.

The particle-level jets are reconstructed from stable final-state particles using the anti-k_T algorithm with radius parameter $R = 0.4$. The particle-level leading jet is required to have $p_T > 21$ GeV and is matched event-by-event to a reconstruction-level jet using a distance of $\Delta R = 0.3$. The generator-level transverse region ΣE_T is defined as summing the transverse energies of stable final-state particles with $|\eta| < 1.1$ in the transverse region as determined by $\Delta\phi$ from the generator-level leading jet. For inclusion in the ΣE_T measurement, stable final-state EM particles are required to have a $p_T > 200$ MeV and final-state hadrons are required to have a $p_T > 500$ MeV. These particle-level p_T thresholds are consistent with those adopted in previous underlying event measurements at RHIC and the LHC [13, 9].

Unfolding is performed using two iterations of the RooUnfold Bayesian iterative unfolding method [36, 37]. Two iterations of unfolding are chosen since any further variation per iteration reached the scale of the bin-by-bin statistical uncertainty. The sensitivity to the prior distributions in this unfolding procedure is also tested by comparing the generator-level prediction and a

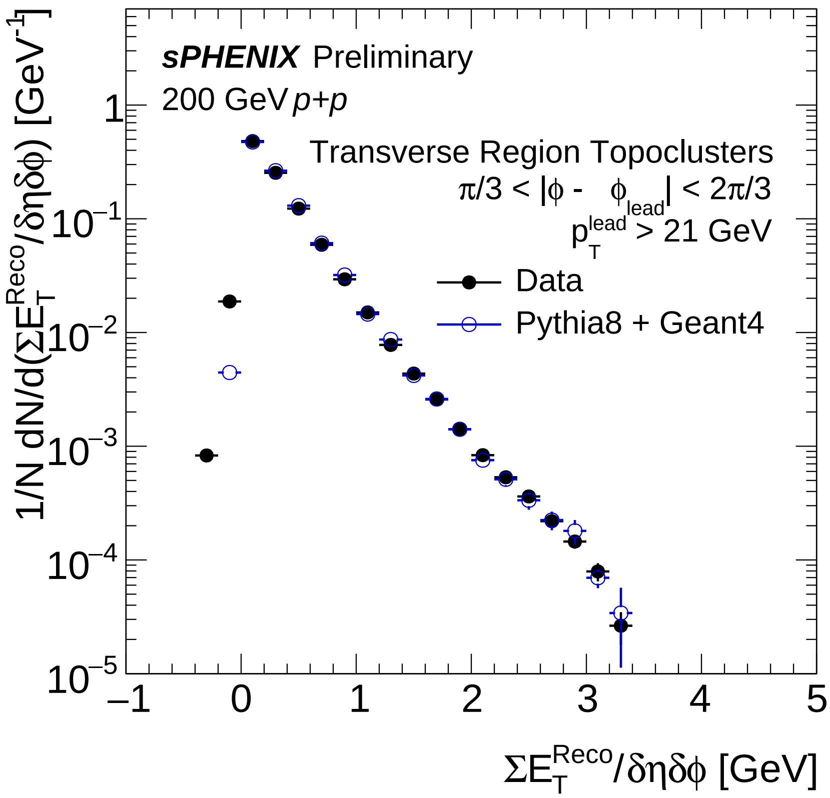

Figure 4: Comparison of reconstruction-level transverse energy density distributions between data (filled black points) and Pythia8+Geant4 simulation (open blue points) for the transverse region defined with respect to the reconstructed leading jet. The leading jet is defined as the highest-p_T jet reconstructed with the anti-k_t algorithm ($R = 0.4$), required to satisfy $p_T^{\text{lead}} > 21$ GeV and $|\eta^{\text{lead}}| < 0.7$. The transverse energy density distributions are calibrated at the electromagnetic (EM) scale. All event and jet quality selections follow those outlined in Section 3.3.

reweighted simulation prior which will be discussed in the next section. The stability of the entire unfolding procedure was quantified via a standard closure test based on the average energy density recovered after being discretized in the response matrix and unfolded for bin migration.

4 Systematic Uncertainties

Systematic uncertainties in this measurement arise from both the jet and calorimeter topocluster observables and are organized into three primary categories: calibration, selection efficiency, and unfolding. The calibration and selection-related uncertainties are evaluated independently for jets and calorimeter topoclusters and subsequently propagated through the full analysis chain, including the unfolding procedure, while the unfolding uncertainties are assessed on the jet and calorimeter topoclusters together. The dominant contributions to the total uncertainty are associated with the calorimeter hadronic response, topocluster noise threshold and unfolding uncertainties.

The leading jet-related calibration uncertainty arises from the data-driven jet energy scale correction, determined from *in-situ* photon–jet and multi-jet balance calibration studies [38], and incorporated via variations of the response matrix used in unfolding. In addition, a systematic variation of the jet energy resolution is also estimated in data from di-jet balancing across different event topologies. More details regarding these specific methodologies are available here: [32]. For the topoclusters, the dominant calibration uncertainty is the hadronic response uncertainty, determined by observed differences between data and simulation in test beam measurements, and implemented as a coherent scale uncertainty on the reconstructed topocluster energies. Other calibration-related effects, including the calorimeter absolute EM energy scale calibration scale and resolution uncertainties, are found to contribute at the percent level or below.

Selection efficiency uncertainties quantify the sensitivity of the measurement to event and object selection criteria. The largest effects in this category arise from variations in the topocluster noise threshold and the treatment of pileup. The noise uncertainty is evaluated by modifying the clustering thresholds in both data and simulation, resulting in variations at the few percent level. The pileup uncertainty is assessed by comparing results obtained with and without the application of a data-driven pileup correction. Additional selection-related uncertainties, such as those associated with jet trigger, MBD vertex reconstruction, and jet timing selection efficiencies, are observed to have a negligible impact on the final results. The systematic uncertainty on the MBD vertex efficiency is estimated from the efficiency scale difference between data and simulation in a low-pileup dijet sample. With regards to event selection, the fit parameters to the jet trigger are varied within 1σ uncertainties and the resulting systematic uncertainty is found to be negligible.

Unfolding uncertainties account for the sensitivity of the corrected distributions to the modeling of the detector response and the choice of prior. The first contribution arises from prior reweighting, evaluated by comparing results with and without reweighting of the input distribution used in the unfolding procedure. A variation using an alternative generator, Herwig7.3, for the response matrix formation is is used to evaluate the model in the unfolding.

The total systematic uncertainty is obtained by summing all variations in the UE observable, $\langle \Sigma E_T / \delta\eta\delta\phi \rangle$, in quadrature for each leading jet p_T bin. The calibration and selection efficiency uncertainties are evaluated independently for the jet and calorimeter topocluster observables and subsequently propagated through the full unfolding procedure, while the unfolding uncertainties are assessed on the combined jet and topocluster response. This independent treatment is well-motivated given that the dominant uncertainty contributions arise from the hadronic response, pileup, and noise threshold effects on the low-energy topoclusters, which are less precisely constrained than the jet energy scale and resolution. All variations are evaluated both upward and downward, with the exception of the unfolding, pileup correction, and topocluster resolution uncertainties, which are one-sided. The values of the systematic variations for the inclusive jet and dijet event results are given in Table 1.

5 Results

Figure 5 presents the unfolded average total transverse energy density, $\langle \Sigma E_T / \delta\eta\delta\phi \rangle$, in the transverse region across the full calorimeter η acceptance, $|\eta| < 1.1$, as a function of the leading jet

Source	Inclusive Jet Events	Dijet Events
Jet energy scale	+0.9/-0.6	-0.6
Jet energy resolution	+1.0/-0.7	+0.1/-0.5
Topocluster pileup correction	-2.7	-2.5
Topocluster EM scale calibration	+1.5/-1.5	+1.5/-1.4
Topocluster hadronic response	+4.4/-4.7	+4.6/-4.6
Topocluster resolution	+0.1	+<0.1
Topocluster noise threshold	+3.6/-2.7	+3.8/-2.3
MBD vertex efficiency	+1.0/-1.2	+1.1/-1.2
Unfolding	+3.5	+2.2
Total	+8.2/-6.6	+7.5/-6.5

Table 1: Average value across jet p_T bins for systematic uncertainties for inclusive jet and dijet events. The $+$ and $-$ values represent the upward and downward variations, respectively, of $\langle \Sigma E_T / \delta\eta\delta\phi \rangle$ averaged over the full range of jet p_T bins for the given systematic source. All uncertainty values are given in percentage (%).

transverse momentum for both inclusive jet and dijet event selections. The results are compared to generator-level predictions from Pythia8 and Herwig7.

A consistent trend is observed in both event selections: the underlying event transverse energy density decreases with increasing leading jet p_T. The systematic uncertainties are strongly correlated across jet p_T bins, meaning that the shape of the distributions are precisely constrained. Additionally, the inclusive jet and dijet measurements are in agreement within their uncorrelated uncertainties, indicating that the observed anti-correlation is not significantly sensitive to requiring a dijet event selection at RHIC energies. This is in contrast to observations at the LHC, where measurements show a reduced or slightly negative dependence of UE activity on the hard scale in dijet events compared to the positive trend seen in inclusive jet events [9]. Since mid-rapidity reconstructed jets at RHIC energies are initiated by partons higher x, as compared to jets at the LHC, the impact of the di-jet selection is conceptually different when comparing across collision energies. Therefore, the two sets of data can be utilized to simultaneously tune various MC models accurately.

The observed decrease of UE activity with increasing jet p_T indicates a consistent and non-trivial correlation between the hard scattering scale and soft particle production at RHIC energies. As already described earlier, one might naively expect that the underlying event and higher-Q^2 scatterings are positively correlated since one expects increased initial- and final-state radiation and a preferential selection of events with larger overlap of the colliding nucleons, enhancing the probability of MPI. Instead, here the UE transverse energy density decreases with increasing jet p_T, consistent across both inclusive jet and dijet selections. This suggests that the interplay between soft and hard processes at RHIC energies is more subtle than a simple scaling of total emissions from both perturbative (wide angle emissions from jets) and non-perturbative (MPI) with the hard scattering scale. The soft and hard particle production processes occurring in collisions at RHIC energies are kinematically coupled at large parton momentum fraction. This kinematic coupling, along with energy-momentum conservation imposes an important constraint on the UE which is not as strong at higher collision energies due to a smaller x on average. This observable may also be sensitive to PDF effects in RHIC-versus-LHC comparisons, since the differing quark and gluon

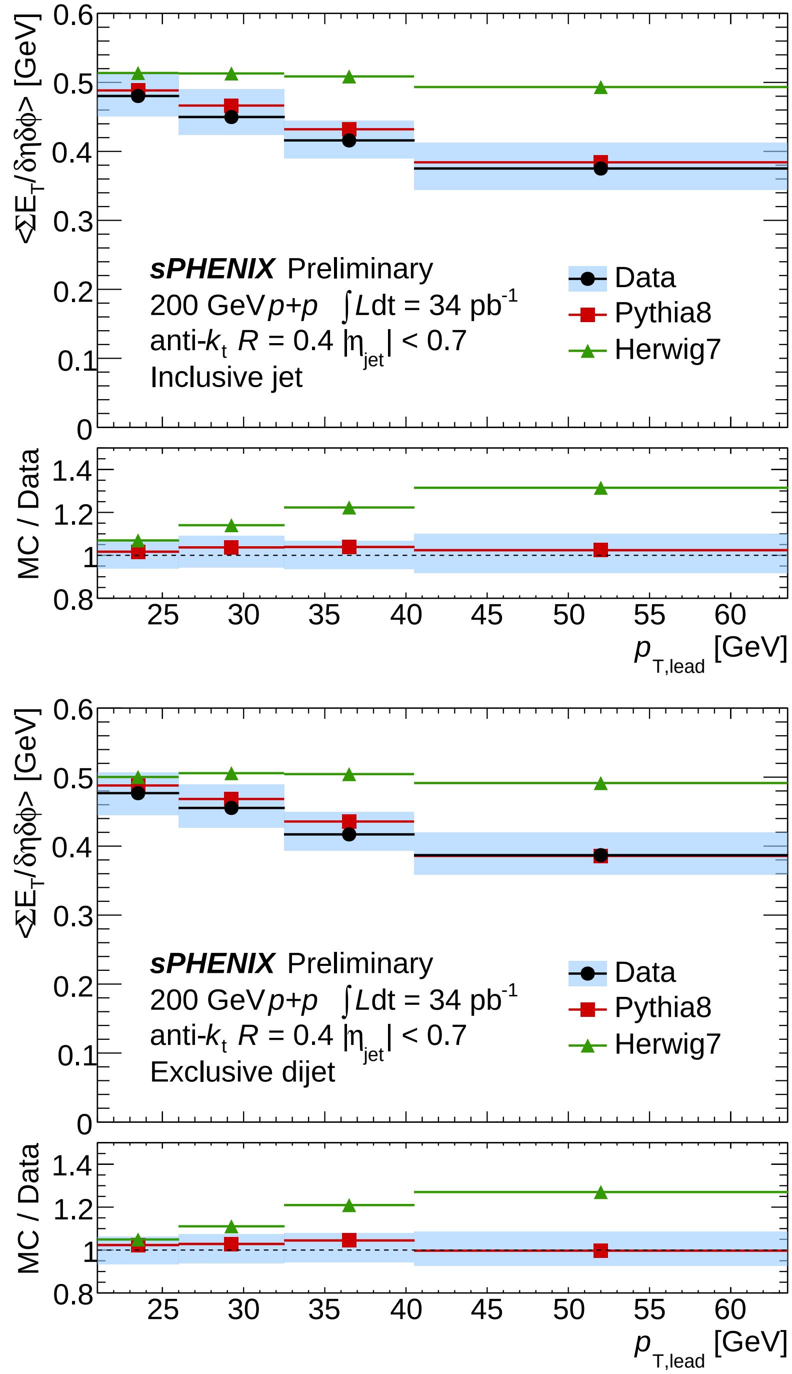

Figure 5: $\langle \Sigma E_T / \delta\eta\delta\phi \rangle$ in the transverse region across full calorimeter η acceptance as a function of leading jet p_T for inclusive jet (left) and dijet (right) event selections. Data (black points) are shown with statistical uncertainties (bars) and systematic uncertainties (blue bands). The results are compared to generator-level predictions from RHIC tuned Pythia8 Detroit tune (red squares) and Herwig7 Nashville tune (green triangles). The bottom panels show the ratio of each generator prediction to the data.

fractions probed at RHIC and LHC change the flavor of the jet-initiating parton, which in turn modifies the associated wide-angle radiation.

Comparisons to Pythia8 show that the generator reproduces the observed decreasing trend of UE activity with jet p_T. In contrast, Herwig7 predicts an approximately constant UE activity as a function of jet p_T, in disagreement with the data, with the discrepancy becoming most pronounced at high jet p_T. Both Pythia8 and Herwig7 incorporate MPI through an impact-parameter-dependent framework and include initial- and final-state radiation tied to the hard scattering scale. However, a key distinction lies in how the interplay between these components is modeled. In Pythia8, MPI are interleaved with parton shower evolution in a common p_T-ordered sequence, introducing a dynamical and tunable competition between soft and hard processes. This framework allows the relative contributions of MPI and radiation to evolve with the event kinematics, leading to a correlated dependence of UE activity on the leading jet p_T. In contrast, Herwig7 treats multiple MPI and parton shower evolution in a more factorized manner, without an explicit interleaved competition between soft and hard components. As a result, the underlying event activity is more weakly coupled to the hard scattering scale. The sensitivity of the present measurement to the evolution of UE activity with jet p_T therefore provides a discriminating test of these modeling approaches and places important constraints on the description of soft–hard interplay in $p+p$ collisions at RHIC energies.

Finally, the sPHENIX results are compared directly with STAR in Fig 6. The left side y-axis of the figure shows the average charge density, $\langle \delta N_{ch}/\delta\eta\delta\phi \rangle$, from STAR with the right side of the axis showing the energy density from this measurement. The conversion from the number density to the energy density is not straightforward, therefore we have scaled the y-axies to have the point at jet $p_T = 35$ GeV roughly matching between sPHENIX and STAR to emphasize the shape comparison. There is a negative slope of both datasets with the STAR measurement focused on the lower jet momenta with no significant trend of the correlation after jet $p_T \geq 15$ GeV where this measurement increased the significance of the slope to higher jet momenta. The comparison between the datasets is especially important to reveal this anti-correlation persisting to higher jet momenta.

6 Summary

A measurement of the correlation between the underlying event production and the leading jet transverse momentum in $p+p$ collisions at $\sqrt{s} = 200$ GeV has been presented using the sPHENIX detector. The analysis utilizes calorimeter topoclusters to reconstruct soft particle production in regions azimuthally transverse to the leading jet and the final results are presented after a multi-dimensional unfolding procedure to correct for detector effects.

The underlying event density per unit area, $\langle \Sigma E_T/\delta\eta\delta\phi \rangle$, is measured as a function of the leading jet transverse momentum for both inclusive jet and dijet event selections. A consistent decrease of the transverse energy density with increasing jet p_T is observed in both selections, demonstrating a clear correlation between the hard scattering scale and soft particle production at RHIC energies. This behavior differs from the naive expectation that higher-Q^2 scatterings lead to increased underlying event activity through enhanced radiation and MPI. The agreement between inclusive and dijet results indicates that this trend is robust with respect to the event topology at RHIC

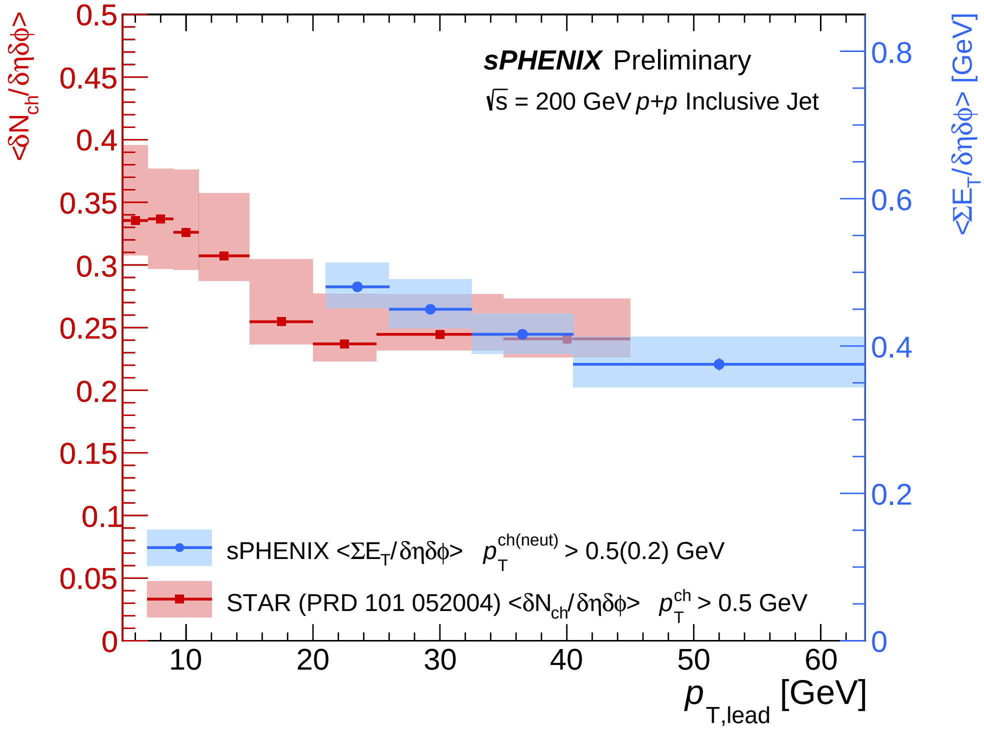

Figure 6: Comparison of the underlying-event activity in the transverse region between sPHENIX and STAR [13] as a function of leading jet p_T. The left axis shows the charged-particle density, $\langle dN_{\mathrm{ch}}/\delta\eta\delta\phi\rangle$, corresponding to the STAR results (red squares), and the right axis shows the transverse energy density, $\langle \Sigma E_T/\delta\eta\delta\phi\rangle$, corresponding to the sPHENIX results (light blue circles), over the range $5 < p_T^{\mathrm{lead}} < 63$ GeV. An axis scaling of 1.7 is used to overlay the STAR $\langle \delta N_{\mathrm{ch}}/\delta\eta\delta\phi\rangle$ and sPHENIX $\langle \Sigma E_T/\delta\eta\delta\phi\rangle$ results.

collision energies. These results provide insight into the correlation mechanism via energy conservation between the hard and soft scattering processes.

Comparisons to Pythia8 and Herwig7 highlight the importance of modeling the interplay between MPI and perturbative radiation including parton showers. While both generators incorporate impact-parameter-dependent MPI and radiation tied to the hard scale, they differ in how these components are combined. The observed sensitivity of the underlying event to the leading jet p_T strongly favors models in which soft and hard processes are dynamically coupled, such as in Pythia8, at a significant level within uncertainties, and provides new constraints on event generator descriptions of the underlying event at RHIC energies.

This measurement establishes a baseline for future studies of the underlying event in small systems and motivates further investigation of the mechanisms governing soft particle production and its connection to hard processes at RHIC energies.

References

[1] P. Bartalini and J. R. Gaunt. *Multiple Parton Interactions at the LHC*, volume 29 of *Advanced Series on Directions in High Energy Physics*. World Scientific, Singapore, 2018. doi:10.1142/10646. 1

[2] M. Diehl and J. R. Gaunt. Double parton scattering theory overview. *Adv. Ser. Direct. High Energy Phys.*, 29:7–28, 2018. doi:10.1142/9789813227767_0002. 1

[3] T. Sjöstrand. The Development of MPI Modeling in Pythia. *Adv. Ser. Direct. High Energy Phys.*, 29:191–225, 2018. arXiv:1706.02166, doi:10.1142/9789813227767_0010. 1

[4] A. Buckley et al. General-purpose event generators for LHC physics. *Phys. Rept.*, 504:145–233, 2011. doi:10.1016/j.physrep.2011.03.005. 1

[5] J. L. Nagle and W. A. Zajc. Small System Collectivity in Relativistic Hadronic and Nuclear Collisions. *Ann. Rev. Nucl. Part. Sci.*, 68:265–294, 2018. arXiv:1801.03477, doi:10.1146/annurev-nucl-101916-123209. 1

[6] W. Busza, K. Rajagopal, and W. van der Schee. Heavy Ion Collisions: The Big Picture and the Big Questions. *Annual Review of Nuclear and Particle Science*, 68:339, 2018. doi:10.1146/annurev-nucl-101917-020852. 1

[7] R. K. Ellis, W. J. Stirling, and B. R. Webber. *QCD and Collider Physics*, volume 8 of *Cambridge Monographs on Particle Physics, Nuclear Physics and Cosmology*. Cambridge University Press, 1996. doi:10.1017/CBO9780511628788. 1

[8] L. Frankfurt, M. Strikman, and C. Weiss. Transverse nucleon structure and diagnostics of hard parton-parton processes at LHC. *Phys. Rev. D*, 83:054012, 2011. doi:10.1103/PhysRevD.83.054012. 1

[9] ATLAS Collaboration. Measurement of the underlying event in jet events from 7 TeV proton–proton collisions with the ATLAS detector. *Eur. Phys. J. C*, 74:2965, 2014. arXiv:1406.0392, doi:10.1140/epjc/s10052-014-2965-5. 1, 3.3, 3.5, 5

[10] ALICE Collaboration. Underlying event measurements in pp collisions at $\sqrt{s} = 0.9$ and 7 TeV with the ALICE experiment at the LHC. *Journal of High Energy Physics*, 07:116, 2012. arXiv:1112.2082, doi:10.1007/JHEP07(2012)116. 1

[11] ATLAS Collaboration. Measurement of distributions sensitive to the underlying event in inclusive Z-boson production in pp collisions at $\sqrt{s} = 7$ TeV with the ATLAS detector. *The European Physical Journal C*, 74:3195, 2014. arXiv:1409.3433, doi:10.1140/epjc/s10052-014-3195-6. 1

[12] CDF Collaboration. Studying the underlying event in Drell-Yan and high transverse momentum jet production at the Tevatron. *Physical Review D*, 82:034001, 2010. doi:10.1103/PhysRevD.82.034001. 1

[13] STAR Collaboration. Underlying event measurements in p+p collisions at $\sqrt{s} = 200$ GeV at RHIC. *Phys. Rev. C*, 101:052004, 2020. doi:10.1103/PhysRevD.101.052004. 1, 3.5, 6

[14] STAR Collaboration. Correlations of event activity with hard and soft processes in $p+$Au collisions at $\sqrt{s_{NN}} = 200$ GeV at the rhic star experiment. *Phys. Rev. C*, 110(4):044908, 2024. doi:10.1103/PhysRevC.110.044908. 1

[15] M. Kordell and A. Majumder. Jets in d(p)-A Collisions: Color Transparency or Energy Conservation. *Phys. Rev. C*, 97(5):054904, 2018. doi:10.1103/PhysRevC.97.054904. 1

[16] ATLAS Collaboration. Measurement of the dependence of transverse energy production at large pseudorapidity on the hard-scattering kinematics of proton–proton collisions at $\sqrt{s} = 2.76$ TeV with ATLAS. *Phys. Lett. B*, 756:10–28, 2016. arXiv:1512.00197, doi:10.1016/j.physletb.2016.02.056. 1

[17] A. Adare et al. An upgrade proposal from the PHENIX Collaboration, 2015. arXiv:1501.06197. 1, 2

[18] R. Belmont et al. Predictions for the sPHENIX physics program. *Nucl. Phys. A*, 1043:122821, 2024. doi:10.1016/j.nuclphysa.2024.122821. 1

[19] C. Bierlich et al. A comprehensive guide to the physics and usage of PYTHIA 8.3. *SciPost Phys. Codeb.*, 2022:8, 2022. arXiv:2203.11601, doi:10.21468/SciPostPhysCodeb.8. 1, 3.2

[20] M. R. Aguilar et al. Pythia8 underlying event tune for RHIC energies. *Phys. Rev. D*, 105(1):016011, 2022. arXiv:2110.09447, doi:10.1103/PhysRevD.105.016011. 1, 3.2

[21] J. Bellm et al. Herwig 7.0/Herwig++ 3.0 release note. *The European Physical Journal C*, 76(4), 2016. URL: http://dx.doi.org/10.1140/epjc/s10052-016-4018-8, doi:10.1140/epjc/s10052-016-4018-8. 1, 3.2

[22] U. S. Qureshi et al. New Herwig7 underlying event tune: From RHIC to LHC energies. *Physical Review D*, 112(11), 2025. URL: http://dx.doi.org/10.1103/cnck-wtbh, doi:10.1103/cnck-wtbh. 1, 3.2

[23] M. Harrison, T. Ludlam, and S. Ozaki. RHIC project overview. *Nucl. Instrum. Meth. A*, 499(2):235–244, 2003. doi:10.1016/S0168-9002(02)01937-X. 2

[24] C. A. Aidala et al. Design and Beam Test Results for the 2-D Projective sPHENIX Electromagnetic Calorimeter Prototype. *IEEE Transactions on Nuclear Science*, 68(2):173–181, 2021. doi:10.1109/TNS.2020.3034643. 2, 3.4.1

[25] C. A. Aidala et al. Design and Beam Test Results for the sPHENIX Electromagnetic and Hadronic Calorimeter Prototypes, 2018. arXiv:1704.01461. 2, 3.4.1

[26] T. G. O'Connor et al. Design and testing of the 1.5 T superconducting solenoid for the BaBar detector at PEP-II in SLAC. *IEEE Trans. Appl. Supercond.*, 9:847–851, 1999. doi:10.1109/77.783429. 2

[27] K. Ikematsu et al. A Start - timing detector for the collider experiment PHENIX at RHIC-BNL. *Nucl. Instrum. Meth. A*, 411:238–248, 1998. arXiv:physics/9802024, doi:10.1016/S0168-9002(98)00307-6. 2

[28] M. Allen et al. PHENIX inner detectors. *Nuclear Instruments and Methods in Physics Research Section A: Accelerators, Spectrometers, Detectors and Associated Equipment*, 499(2):549–559, 2003. The Relativistic Heavy Ion Collider Project: RHIC and its Detectors. doi:10.1016/S0168-9002(02)01956-3. 2

[29] sPHENIX Collaboration. Measurement of the transverse energy density in Au+Au collisions at $\sqrt{s_{NN}} = 200$ GeV with the sPHENIX detector. *Phys. Rev. C*, 112(2):024908, 2025. arXiv:2504.02242, doi:10.1103/h8d5-swg6. 2

[30] sPHENIX Collaboration. Measurement of charged hadron multiplicity in Au+Au collisions at $\sqrt{s_{\mathrm{NN}}}$= 200 GeV with the sPHENIX detector. *JHEP*, 08:075, 2025. arXiv:2504.02240, doi:10.1007/JHEP08(2025)075. 2

[31] S. Agostinelli et al. GEANT4–a simulation toolkit. *Nucl. Instrum. Meth. A*, 506:250–303, 2003. doi:10.1016/S0168-9002(03)01368-8. 3.2

[32] sPHENIX Collaboration. Measurement of dijet transverse momentum imbalance and azimuthal acoplanarity in $p + p$ collisions at $\sqrt{s} = 200$ GeV with the sPHENIX detector, 2026. arXiv:2606.17184. 3.3, 4

[33] M. Cacciari, G. P. Salam, and G. Soyez. The anti-k_t jet clustering algorithm. *JHEP*, 04:063, 2008. doi:10.1088/1126-6708/2008/04/063. 3.3

[34] M. Cacciari, G. P. Salam, and G. Soyez. FastJet user manual. *Eur. Phys. J. C*, 72:1896, 2012. doi:10.1140/epjc/s10052-012-1896-2. 3.3

[35] ATLAS Collaboration. Topological cell clustering in the ATLAS calorimeters and its performance in LHC Run 1. *Eur. Phys. J. C*, 77:490, 2017. arXiv:1603.02934, doi:10.1140/epjc/s10052-017-5004-5. 3.4

[36] T. Adye. Unfolding algorithms and tests using RooUnfold, 2011. URL: https://arxiv.org/abs/1105.1160, arXiv:{1105.1160}. 3.5

[37] G. D'Agostini. A multidimensional unfolding method based on bayes' theorem. *Nucl. Instrum. Meth. A*, 362(2):487–498, 1995. doi:10.1016/0168-9002(95)00274-X. 3.5

[38] sPHENIX Collaboration. Precise measurement of jet energy scale derived from in situ techniques using γ-jet and multijet transverse momentum balance in p+p collisions at $\sqrt{s} =$ 200 GeV with the sPHENIX detector. URL: https://www.sphenix.bnl.gov/sites/default/files/2026-06/sPH-CONF-JET-2026-01.pdf. 4